Energy Partitioning and Horizontal Dispersion in a Stratified Rotating Lake*

ROMAN STOCKER

Dipartimento di Ingegneria Idraulica, Marittima, Geotecnica ed Ambientale, Universitá di Padova, Padua, Italy

JÖRG IMBERGER

Centre for Water Research, University of Western Australia, Perth, Australia

(Manuscript received 2 January 2002, in final form 22 August 2002)

ABSTRACT

The response of a stratified rotating basin to the release of a linearly tilted interface is derived. This case is compared with a uniformly forced basin in the two limits when the duration of the forcing is much greater than the period of the dominant internal waves and when it is much smaller. Energy partitioning is studied as a function of the Burger number S (relative importance of stratification versus rotation), showing the dominance of a geostrophic component over the wave field for low S. Trajectories are integrated numerically, revealing the Stokes drift of the waves to be always cyclonic. Transport properties are classified in terms of S and the Wedderburn number W (relative importance of the disturbance versus stratification). The geostrophic flow is the main source of advection, but only the waves allow particles to break the barrier to transport between the two geostrophic gyres, ultimately leading to stretching and folding. For low values of W, advection can become chaotic. Conservation of potential vorticity explains the difference in transport properties between the forced cases and the initial tilt release. A transition time between spreading dominated by turbulence and that dominated by large-scale motions is derived as a function of the initial size of a cloud. The results show that spreading is mainly due to turbulence for weak forcing, small time, and small clouds; for stronger forcing, larger time, or larger clouds the effect of large-scale motions can be dominant.

1. Introduction

It has been established that the energy path transferring mechanical energy from the wind down to the smallest scales of motion in a stratified lake begins with the baroclinic basin-scale motions (Imberger 1998). These are influenced by the earth's rotation even in basins of medium size (Antenucci and Imberger 2001). Their spatial structure is best described in terms of the Burger number S, which accounts for the relative influence of stratification and rotation (Antenucci and Imberger 2001), and the Wedderburn number W, which accounts for the severity of the forcing or initial disturbance with respect to the stratification (Spigel and Imberger 1980). The Burger number is defined here as $S = c/fr_0$, where c is the nonrotational baroclinic phase speed, f the inertial frequency and r_0 the horizontal dimension of the basin. Sometimes, the square of this expression is used (Pedlosky 1979). Antenucci and Imberger (2001) compute ratios of potential to kinetic energy for the dominant natural modes of a circular basin as a function of S. However, the question of how the energy due to an initial disturbance or to a given forcing is partitioned among the different modes has not been addressed. It is the answer to this question that ultimately determines the ratio of potential to kinetic energy in the basin. In particular, the response of a rotating system to external disturbances includes a geostrophic flow (Veronis 1956; Csanady 1968; Gill 1982). Its importance with respect to the wave field has been evaluated for an unbounded ocean by Veronis (1956), who found that the amount of energy entering the geostrophic component increases with the duration of the wind if the total momentum is kept constant. This result will be extended to closed basins.

When a wind blows over a stratified nonrotating lake, an interface tilt is usually generated, causing the thermocline to rise upwind and fall downwind (Monismith 1986). When rotation is negligible ($S \to \infty$) this adjustment happens over a time depending on the size of the basin (Monismith 1985), typically of the order of 10 h for medium size lakes like Lake Kinneret (Israel) (Serruya et al. 1984). When the wind stops blowing, the interface tilt is released, resulting in a seiching motion. The solution for a uniform, constant wind imposed sud-

* Centre for Water Research Reference Number ED 1625-RS.

Corresponding author address: Roman Stocker, Department of Applied Mathematics, MIT, 2-339, 77 Massachusetts Ave., Cambridge, MA 02139.
E-mail: stocker@math.mit.edu

denly over a circular homogeneous rotating basin with flat bottom has been given by Csanady (1968) for the case of a wind lasting much longer than the period of the dominant internal waves (this forced problem will be denoted hereinafter as FP). In the first part of this paper Csanady's solution is extended to a wind duration much shorter than the dominant internal wave's period. An analytical solution to the initial boundary value problem associated with the evolution of a surface tilt in a rotating lake is also derived. The linear initial tilt contains all the Fourier components of the basin's response, therefore representing a general and yet simple condition to be investigated. Furthermore, in a nonrotating lake excited by surface wind forcing the thermocline assumes a linear shape after one-quarter of the period of the gravest internal wave (Spigel and Imberger 1980). Both the forced and the initial boundary value problems (IBVP) are solved for a homogeneous basin, but are readily applicable to stratified problems (with layers of uniform density) by way of normal mode decomposition (Csanady 1967, 1982). The study of energy partitioning among the components of the solution reveals the importance of a geostrophic component, which in the IBVP dominates over the wave field as the Burger number decreases, while it has the same energy as the wave field for all Burger numbers in the FP. This result is compared to that of Veronis (1956). While the variable depth case has been studied by Birchfield and Hickie (1977) and Huang and Saylor (1982) for a homogeneous basin, it appears difficult to extend these results to stratified conditions.

The basin-scale motions are responsible for basinwide redistribution of nutrients, pollutants, and sediments (Ostrovsky et al. 1996; Imberger 1998). This is particularly true for the surface layer of a stratified lake, where most of the biological processes of the lake occur. Despite its importance, little is known about the basic mechanisms governing horizontal transport and dispersion due to basin-scale motions in the surface layer.

Field dispersion studies in a range of environments usually lump all mechanisms responsible for the spreading of a cloud into one empirical law relating the rate of growth of its area (or apparent diffusivity) to a characteristic length scale of the cloud (Okubo 1971; Lawrence et al. 1995). Csanady (1963) finds no correlation whatsoever between diffusion patterns and meteorological data. However, he also observes that ''there are good days and bad days for diffusion.'' While the outcomes of such investigations are of considerable practical usefulness (Lawrence et al. 1995), great care is needed when they are applied to situations different than those for which they were gathered (Fischer et al. 1979), since misinterpretations of the physical processes causing dispersion can arise. This has been shown by Murthy (1975), who found that convergence and divergence of the mean flow field can act as antidiffusive agents undoing the dispersive action of turbulence. Assigning the bulk observed growth of a cloud to turbulent dispersion would lead to a vast underestimate of eddy diffusivity. For confined water bodies like lakes, in particular, this lack of distinction between mean flow effects and turbulence makes it difficult to generalize dispersion experiment results. List et al. (1990) point out the importance of regarding turbulent diffusion as an ensemble average property, due to the doubtful applicability of dispersion theory to single realizations of a dispersion experiment. We suggest that the variability in single realizations is a result not only of the statistical variability of turbulent dispersion, but also of the structure of the underlying velocity field. Csanady (1966) already mentioned this, suggesting that variations in dispersion coefficients can be predominantly linked to spatial and temporal structures of the currents, in particular to their degree of nonuniformity in space and time, and not necessarily to a change in the horizontal eddy structure. This suggests the importance of mesoscale motions not only for advective but also for dispersive processes and points to the necessity of a distinction between different dispersion mechanisms and a quantification of the relative importance of each of them.

The dispersion caused by the mean flow can be profitably studied with the tools of dynamical systems, considering the process as completely deterministic. The existence of unsteady flows whose Eulerian velocity field is deterministic and smooth but nevertheless able to generate complex patterns in terms of particle trajectories is well established (Lichtenberg and Lieberman 1983). Linearization of the equations of motion precludes chaotic behavior of the Eulerian velocity field (*hard chaos*). However, the most intriguing aspect of chaotic advection is the complex stretching and folding of material lines due to the nonlinearity in the integration of trajectories (*weak chaos*) (Cox et al. 1990). Aref (1984) coined the term *chaotic advection* to describe this behavior. By sharpening gradients of concentration of a tracer cloud and effectively increasing its exchange area with the surrounding fluid, chaotic advection strongly favors mixing. The latter is actually achieved through smaller scale processes supported by turbulent dispersion.

The fact that chaotic advection in time periodic flows can be an effective horizontal dispersion mechanism without recourse to turbulence has already been recognized in the estuarine literature (Zimmerman 1986; Ridderinkhof and Zimmerman 1992). Zimmerman (1986) considered the tidal velocity field as composed of a uniform, time periodic flow and a spatially varying residual flow. He ascribed the large dispersion coefficients often observed in estuaries to their strong geometrical complexity, but also recognized that, the flow being time dependent, a single spatial mode perturbing the uniform current would be sufficient to produce chaotic advection. In the absence of complex topography, the perturbing action of a mean flow leading to chaotic advection can be exerted by waves, as shown for example by Cox et al. (1990) and Binson (1997). In these

latter studies, however, only the kinematics were included, the simplified velocity fields being given a priori. The second part of this paper will extend these considerations to the internal waves developing in a rotating basin. While conserving the simplicity of a limited number (one or two) of perturbing modes, the dynamical aspect of the problem will be retained by making use of the Eulerian velocity derived analytically. Poincaré maps and local Lyapunov exponents are introduced to analyze transport properties of the geostrophic component perturbed by the internal waves. The evolution of clouds of particles is studied. A transition time between chaotic advection dominated dispersion and turbulence dominated dispersion is derived.

2. The fundamental solution

The solution for a flat bottomed, circular, rotating basin, filled with a homogeneous nonviscous liquid subject to a linear initial tilt of the surface is derived. To deal with the more general forced case, an impulsively started wind stress acting on the surface is included. The linearized, vertically integrated equations of motion and conservation of mass in polar coordinates are

$$\frac{\partial u}{\partial \tau} - v = -\frac{\partial \eta}{\partial r} + SW_F^{-1}\cos\vartheta \tag{1a}$$

$$\frac{\partial v}{\partial \tau} + u = -\frac{\partial \eta}{r\partial \vartheta} - SW_F^{-1}\sin\vartheta \tag{1b}$$

$$\frac{u}{r} + \frac{\partial u}{\partial r} + \frac{\partial v}{r\partial \vartheta} = -\frac{\partial \eta}{\partial \tau}, \tag{1c}$$

where η is the surface displacement, made dimensionless by the depth of the basin H; u, v are vertically averaged velocities in the radial and tangential direction, respectively, made dimensionless by the nonrotational phase speed $c = (gH)^{1/2}$, where g is the acceleration of gravity; τ is time made dimensionless by the inertial frequency f. The radial coordinate has been made dimensionless by the Rossby radius of deformation $R = c/f = r_0 S$ (Gill 1982), where r_0 is the radius of the basin. The forcing term F acts along the direction $\vartheta = 0$ and is a step function in time:

$$F(\tau) = \begin{cases} 0, & \tau < 0 \\ F, & \tau \geq 0. \end{cases} \tag{2}$$

A Wedderburn number (Spigel and Imberger 1980) for the forcing can be defined as $W_F = gH^2/Fr_0$. The initial condition consists of a linear surface tilt with slope C and zero velocity. In dimensionless variables

$$\eta(r, \vartheta, 0) \equiv \eta_0 = Cr_0 SH^{-1} r\cos\vartheta = SW_C^{-1} r\cos\vartheta \tag{3a}$$

$$u(r, \vartheta, 0) = v(r, \vartheta, 0) = 0, \tag{3b}$$

where a second Wedderburn number $W_C = HC^{-1}r_0^{-1}$ for the initial tilt has been introduced. Both Wedderburn numbers are defined here for a homogeneous basin and will be later extended to the stratified case. Since velocities have been vertically integrated over the depth of the fluid, the only remaining boundary condition prescribes zero radial velocity at the shores, $u(S^{-1}, \vartheta, \tau) = 0$.

The general solution including a linear initial tilt and a sudden constant forcing, derived in the appendix, is

$$n(r, \vartheta, \tau) = (W_C^{-1}Q_C - W_F^{-1}Q_F)\cos\vartheta - (W_C^{-1} - W_F^{-1})\sum_{k=1}^{\infty} a_k D_k A_k \tag{4a}$$

$$u(r, \vartheta, \tau) = S(W_C^{-1} - W_F^{-1}) \times \left[\left(1 - \frac{A_0}{rS}\right)\sin\vartheta - \frac{1}{rS}\sum_{k=1}^{\infty} a_k E_k \frac{A_k - \sigma_k\Delta_k}{1 - \sigma_k^2}\right] \tag{4b}$$

$$v(r, \vartheta, \tau) = S(W_C^{-1} - W_F^{-1}) \times \left[\left(1 - \frac{\Delta_0}{rS}\right)\cos\vartheta - \frac{1}{rS}\sum_{k=1}^{\infty} a_k D_k \frac{\Delta_k - \sigma_k A_k}{1 - \sigma_k^2}\right], \tag{4c}$$

where

$$Q_C = rS - A_0 \tag{5}$$

$$Q_F = -A_0 \tag{6}$$

$$D_k = \cos(\vartheta - \sigma_k\tau) \tag{7}$$

$$E_k = \sin(\vartheta - \sigma_k\tau), \tag{8}$$

and the remaining notation is defined in the appendix. The unforced IBVP is recovered when $W_F \to \infty$. The solution for the FP by Csanady (1968), corrected by Birchfield (1969), is recovered when $W_C \to \infty$. Also of interest is the limit of a uniform stormlike wind blowing for a time much shorter than the dominant natural modes (hereafter denoted by IP). An idealized wind in the form of a single impulse can be mathematically represented by Dirac's delta function. The solution can be found by superimposing two oppositely blowing constant winds starting a time $d\tau$ apart, then letting $d\tau \to 0$ while keeping the amount of momentum transferred $M_\delta = Fd\tau$ constant. Alternatively, one can take the time derivative of the FP solution. The solution is recovered from Eq. (4) by considering only the forced part ($W_C \to \infty$), substituting Eqs. (6), (7), and (8) with

$$Q_F = 0 \tag{9}$$

$$D_k = -\sigma_k \sin(\vartheta - \sigma_k\tau) \tag{10}$$

$$E_k = \sigma_k \cos(\vartheta - \sigma_k\tau), \tag{11}$$

and redefining the forcing Wedderburn number as $W_F = gH^2/M_\delta fr_0$.

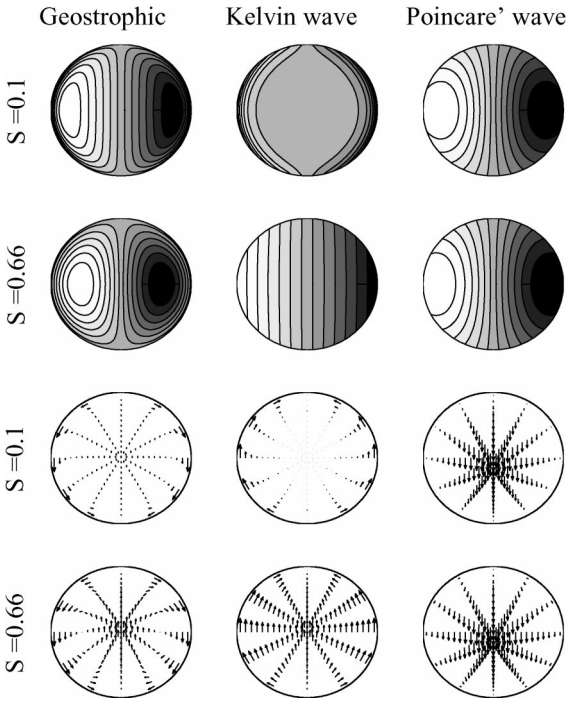

FIG. 1. Instantaneous displacement and velocity field due to the geostrophic component, the Kelvin wave, and the Poincaré wave arising from the IBVP for $S = 0.1$ and $S = 0.66$.

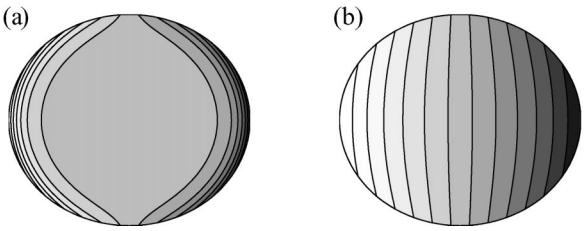

FIG. 2. Geostrophic displacement field due to the FP for (a) $S = 0.1$ and (b) $S = 0.66$.

3. The dominant components of the circulation

a. The wave field

The time-independent term on the rhs of Eq. (4) represents a geostrophic component and the series extending over the infinite natural modes of the basin represents cyclonic and anticyclonic progressive waves. Traditionally, waves with $|\sigma_k| < 1$ have been called Kelvin waves, while those with $|\sigma_k| > 1$ have been called Poincaré waves. According to this definition, the number of Poincaré waves is always infinite. For $S < 1/\sqrt{2}$ one single Kelvin wave exists, while for $S > 1/\sqrt{2}$ there is none (Lamb 1932). However, since the energetic properties associated with the lowest mode wave change smoothly across the boundary $|\sigma_k| = 1$, as will be seen in section 3b, and the direction of rotation remains cyclonic, we will retain the name Kelvin wave for the lowest mode also for $S > 1/\sqrt{2}$. The term Poincaré wave will be reserved in the following for the lowest frequency Poincaré wave. Their natural frequencies can be found through the following fitted relations for $0.1 < S < 2.0$:

$$\sigma_1 = 0.081\,56S^4 - 0.442\,65S^3 + 0.901\,16S^2 + 0.970\,33S - 0.001\,206 \quad (12a)$$

$$\sigma_2 = -0.173\,27S^4 + 0.879\,78S^3 - 1.625\,71S^2 - 0.474\,32S - 0.960\,354 \quad (12b)$$

for the Kelvin wave and first Poincaré wave, respectively. Since the initial condition is an azimuthal mode one displacement and the forcing is uniform in space, all waves have azimuthal mode one (Csanady 1968) and only their radial structure differs, as described by A_k and Δ_k: thus, they can be called *radial* modes. All radial modes are excited both in the IBVP, as the linear tilt cannot be decomposed in a finite number of natural wavelike modes, and in the FP, as the wind starts impulsively. For the IBVP, Fig. 1 shows displacements and velocities of the Kelvin wave and the first Poincaré wave for two values of the Burger number.

Since the influence of the Kelvin wave extends to a distance from the shore comparable to the Rossby radius of deformation, when S is small the Kelvin wave becomes a *coastal jet* (Csanady 1967), with almost negligible radial velocities. The Poincaré wave, on the other hand, affects predominantly the center of the lake and is characterized by a larger radial velocity component. These considerations also hold for the wave field in the FP. The latter differs from the IBVP only with respect to geostrophic displacements, as shown by $Q_C \neq Q_F$, from Eqs. (5) and (6). In the IBVP streamlines of the geostrophic flow follow lines of constant surface elevation since no forcing is present (Fig. 1). In the FP (Fig. 2), when rotation is unimportant, the geostrophic displacements reduce to a linear setup, while the response is pushed to the boundaries when rotation is dominant.

Since no friction has been included in the analysis, both the stationary and the infinite set of wavelike components do not decay with time. Thus, the present solution can be considered to describe the wave field in a real basin for a time proportional to the observed lifetime of internal waves, which is of the order of several days (Mortimer 1952; Ivey and Maxworthy 1992; Antenucci and Imberger 2001). This, however, does not necessarily apply to the geostrophic component, which could be substantially longer lived than the waves.

b. Energy partitioning

Antenucci and Imberger (2001) compute ratios of potential to kinetic energy for the dominant natural modes of a circular rotating basin as a function of the Burger number. Their analysis can be generalized to the present solutions, which include the geostrophic circulation, allowing the partitioning of energy to be determined as

a function of the initial condition or forcing. Because of the circular symmetry of the basin, each radial mode preserves its shape in time. This is not true, for instance, for an elliptic basin (Antenucci and Imberger 2001) and implies that for each mode the energy integrated over the basin is constant and can be computed for example at time zero. Thus, the potential and kinetic energies of the kth radial mode are

$$\mathrm{PE}_k = \int_0^{2\pi}\int_0^{S^{-1}}\int_0^{1+\eta_{k,0}} \rho g z\, dz r\, dr\, d\vartheta = \frac{\rho g}{2}\int_0^{2\pi}\int_0^{S^{-1}} (1+\eta_{k,0})^2 r\, dr\, d\vartheta = \frac{\rho g}{2}\int_0^{2\pi}\int_0^{S^{-1}} \eta_{k,0}^2 r\, dr\, d\vartheta \quad (13)$$

$$\mathrm{KE}_k = \int_0^{2\pi}\int_0^{S^{-1}}\int_0^{1+\eta_{k,0}} \frac{\rho}{2}(u_{k,0}^2 + v_{k,0}^2)\, dz r\, dr\, d\vartheta = \frac{\rho}{2}\int_0^{2\pi}\int_0^{S^{-1}} (u_{k,0}^2 + v_{k,0}^2) r\, dr\, d\vartheta, \quad (14)$$

where $\eta_{k,0}$, $u_{k,0}$, and $v_{k,0}$ are the displacements and velocities of the kth radial mode at time zero and $k = 0$ can be thought of as the geostrophic component. The background potential energy has been neglected and the integral of $\eta_{k,0}$ vanishes because of volume conservation. In Fig. 3, the distribution of energies among the dominant components of the solution to the IBVP (geostrophic component, Kelvin wave, and Poincaré wave) is represented as a function of the Burger number.

Energies are normalized by the potential energy of the initial tilt and higher modes are negligible for all values of S. The partitioning of energy into potential and kinetic is also shown for each component. A further distinction of the kinetic energy in radial and azimuthal is made since this gives an indication of the relative importance of cross-shore versus alongshore velocities.

The rotationless case is recovered from Eq. (4) when $S \to \infty$. For all values of W_C and W_F, the geostrophic velocity field vanishes since in (4) $\lim_{S\to\infty} A_0 = \lim_{S\to\infty} \Delta_0 = rS$ (Abramowitz and Stegun 1965). The equivalence between kinetic and potential energy (Gill 1982) is recovered (Figs. 3 and 4).

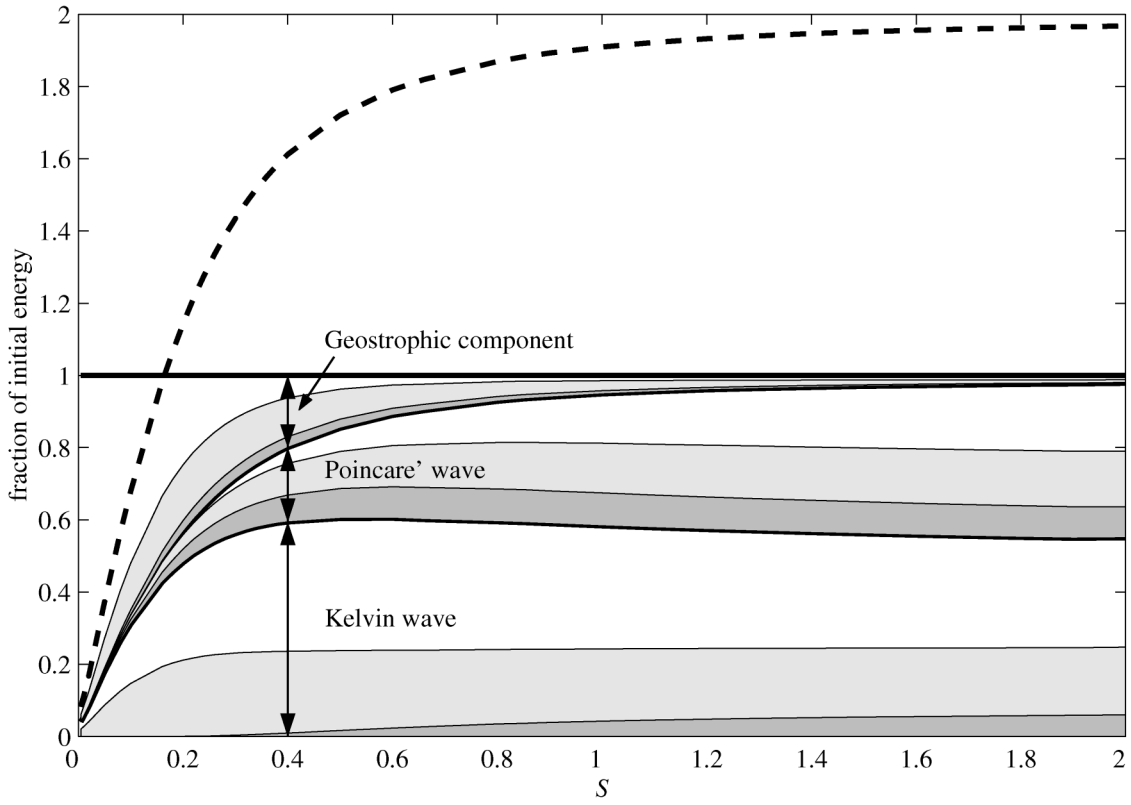

FIG. 3. Partitioning of energy among the Kelvin wave, Poincaré wave, and geostrophic component of the solution to the IBVP as a function of the Burger number S. For each component, the dark gray region represents radial kinetic energy, the light gray region is azimuthal kinetic energy, and the white region is potential energy. Energies are normalized by the initial potential energy. Note that the sum of the energies of the three components is very close to 1. The thick dotted line represents the total energy for the FP, for which all other lines apply unchanged.

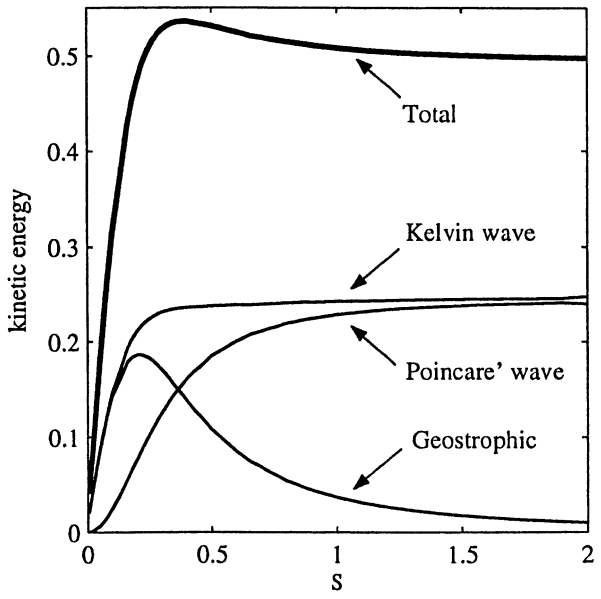

FIG. 4. Kinetic energy of the Kelvin wave, the Poincaré wave, the geostrophic component, and their sum (''Total'') for the IBVP as a function of the Burger number *S*. Energies are normalized by the initial potential energy.

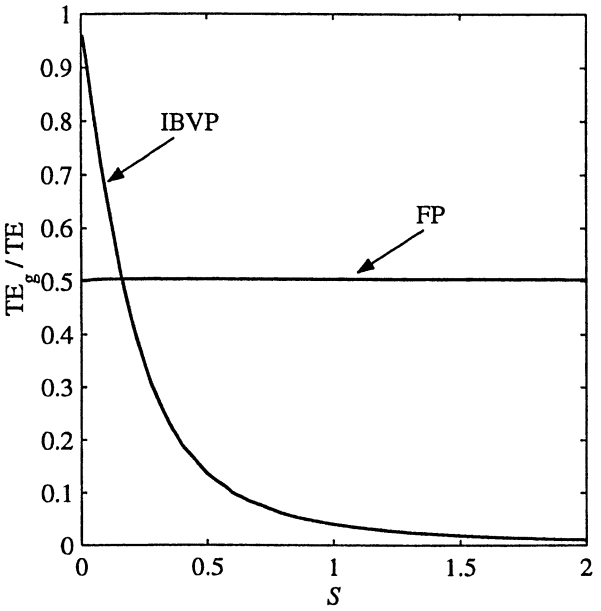

FIG. 5. Total energy of the geostrophic component (TE_g) normalized by the total energy of the response (TE) as a function of the Burger number *S* for the IBVP and the FP. The IBVP closely satisfies the relation $TE_g/TE = e^{-4S}$.

The wave field reduces to simple seiching because the Kelvin and Poincaré wave amplitudes become equal and their frequencies equal and opposite. In the FP the geostrophic displacements become linear for large *S* (Fig. 2), reducing to the rotationless linear setup (Monismith 1985) with no associated circulation (Fig. 3). Half of the total energy goes into wavelike motions and half into the geostrophic motion (Fig. 5).

This latter consideration applies to the FP for all values of *S*. For the IBVP, on the other hand, the geostrophic component vanishes altogether as $S \to \infty$. A best fit from Fig. 5 reveals that the total geostrophic energy TE_g, normalized by the total energy in the response TE, varies with the Burger number as $TE_g/TE = e^{-4S}$. Indeed, in the IBVP the geostrophic displacements adjust so as to conserve the energy provided by the initial tilt.

When rotation is important, the equilibrium position is not the horizontal plane anymore and this involves the existence of a geostrophic circulation. The presence of the geostrophic circulation has been detected at steady state in numerical simulations of homogeneous wind-forced Lake Kinneret by Serruya et al. (1984) and Herman (1989). Both the presence of the two gyres forming the geostrophic circulation (Fig. 2) and their orientation are in good agreement with the present results (see, e.g., Fig. 4 of Serruya et al. 1984). As reported by Herman (1989), Landsat images of a *peridinium* bloom in Lake Kinneret show a remarkable resemblance to the two-gyre configuration. The latter also possibly plays a role in the sediment redistribution in the lake (Herman 1989).

When the response is governed by rotation ($S \to 0$), the contribution of the Poincaré wave becomes negligible (Fig. 6) and the response is dominated by the Kelvin wave and the geostrophic component. The fact that overall kinetic energy vanishes (Fig. 4) agrees with the general conclusion by Gill (1982) that it is difficult to convert potential to kinetic energy in rotating flows.

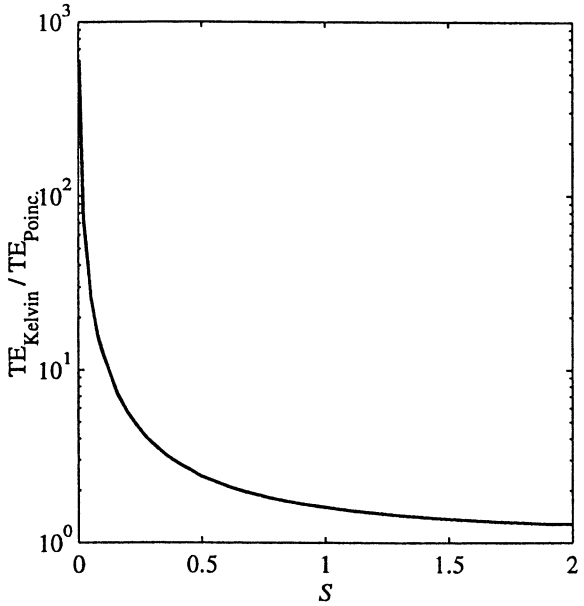

FIG. 6. Ratio of the total energy of the Kelvin wave to the total energy of the Poincaré wave as a function of the Burger number *S*.

For the FP, as $S \rightarrow 0$, the total energy in the response tends to zero, but the equivalence between geostrophic and ageostrophic energy remains (Fig. 5).

At intermediate value of S, when there is a balance between stratification and rotation, both the geostrophic circulation and the two waves are important and the kinetic energy becomes larger than the potential energy (Fig. 4). The spatial scales of the two waves become comparable, since the Rossby radius is comparable with the radius of the basin, implying the influence of the Kelvin wave extends to the interior of the lake.

c. A very short wind

Equation (4), together with Eqs. (9), (10), and (11), shows that brief storm events do not generate any geostrophic motion. It is concluded that the geostrophic component is present only during times when the wind is actually blowing. This agrees qualitatively with the energy partition between geostrophic and wavelike motions for an unbounded ocean (Veronis 1956), where the amount of energy in the geostrophic component increases with the duration of the wind if the total momentum is constant: for an impulsive wind, a wind lasting half an inertial period and a wind lasting one inertial period, the energy in the geostrophic component is 26%, 51%, and 91%, respectively, of the total energy (Veronis 1956).

All natural modes are excited [Eqs. (10) and (11)], as previously, but now amplified in proportion to their frequency. Since Poincaré waves have higher frequencies than Kelvin waves, the importance of the former with respect to the latter is increased when the wind duration becomes shorter. This, together with the stronger radial velocities exhibited by Poincaré waves (Fig. 4), implies that shorter winds favor on- and offshore transport.

d. Conservation of potential vorticity

Despite the fact that the velocity field is the same for the IBVP and the FP, as long as W_C and W_F are equal and opposite, the apparently minor modification in the geostrophic displacements really reflects a deep difference in their long-term transport properties, whose implications can be elegantly interpreted in terms of potential vorticity conservation. The potential vorticity P for a shallow homogeneous layer of depth H is defined as (Gill 1982)

$$P = \frac{f + \zeta}{H + \eta}, \tag{15}$$

where

$$\zeta = \frac{\partial u_y}{\partial x} - \frac{\partial u_x}{\partial y} \tag{16}$$

is the relative vorticity and (u_x, u_y) are the Cartesian components of velocity. In geophysical flows potential vorticity is conserved by each fluid column (Gill 1982), resulting in

$$\frac{DP}{Dt} = \frac{\partial P}{\partial t} + u_x\frac{\partial P}{\partial x} + u_y\frac{\partial P}{\partial y} = 0. \tag{17}$$

This is true also for the uniformly forced problems considered here since the wind stress has zero curl. It is easy to show that the linear velocity field in Eq. (1) satisfies $\partial P/\partial t = 0$. In both forced problems (FP and IP), the nonlinear terms representing advection of potential vorticity in Eq. (17), are identically equal to zero since the spatial gradients of potential vorticity are zero. This implies that the linear velocity field satisfies the nonlinear evolution equation of potential vorticity [Eq. (17)]. The same is not true for the IBVP, where the initial tilt provides a background potential vorticity gradient $\partial P/\partial x \neq 0$. Thus, advection of potential vorticity is not zero, but only a higher-order contribution with respect to the local rate of change $\partial P/\partial t$. As soon as a fluid column moves, it changes relative vorticity in order to conserve potential vorticity. Relative vorticity then gives rise to a velocity field that is usually in the form of a swirling flow or eddy. There appears to be no simple analytical way of determining this velocity field from the initial linear potential vorticity distribution. The mechanism described here has been nicely captured in laboratory experiments by Wake and coworkers, who observed the formation of eddies after a time on the order of 15 inertial periods (G. W. Wake 2001, personal communication).

e. Extension of the solution to two layers

The homogeneous case is readily extended to a two- or three-layer stepwise stratification by normal mode decomposition. Csanady (1967, 1982) gives expressions for the required transformation matrices. The concept underlying normal mode decomposition is that, by taking a suitable combination of the variables for the n layer problem, this can be transformed in n independent problems, each characterized by the same equations as above but with separate Burger numbers. The combination of layer variables is called a normal mode variable. The focus being on surface layer velocities and interface displacements in a two-layer case and since the effect of normal mode two is dominant, the relevant transformations have been carried out explicitly for this case. Let h_j and ρ_j denote the depth and density, respectively, of the jth layer, where $j = 1$ denotes the upper layer and $j = 2$ the lower layer. Further, $H = h_1 + h_2$ and $\varepsilon = 1 - \rho_1/\rho_2$. It can be shown that Eq. (4) can be used with u, v representing surface layer velocities and $-\eta$ representing interface displacements. Here S is replaced by

$$S_2 = \frac{1}{fr_0}\sqrt{g\varepsilon h_1 h_2/H}, \tag{18}$$

where the index 2 points out that only the effect of

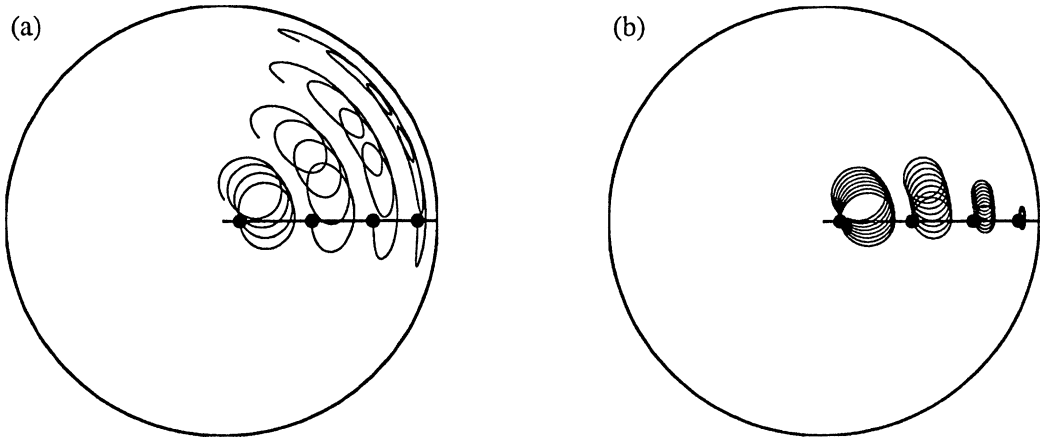

FIG. 7. Particle paths due to (a) the Kelvin wave and (b) the Poincaré wave generated from the IBVP for $S = 0.66$ and $W = 1.4$. Full circles indicate starting positions and trajectories are plotted for 4.4 inertial periods.

normal mode two is considered, and the two-layer version of the Wedderburn numbers is used:

$$W_C = \frac{h_1}{C_2 r_0} \tag{19}$$

$$W_F = \frac{\varepsilon g h_1^2}{F r_0}. \tag{20}$$

It follows that velocities in the surface layer scale as $S_2 W^{-1}$ and interface displacements as W^{-1}. Note that upwelling occurs for $W < 1$ (Spigel and Imberger 1980).

4. Particle trajectories

Armed with the analytical expression for the Eulerian velocity field derived in section 2, we are now in the position to determine the trajectories of particles and to use them, in the following sections, to study the spreading properties of the flow and to compare them with turbulent dispersion.

The trajectory $\mathbf{x}(t)$ of a passive particle starting at $\mathbf{x}_*$ in a Eulerian velocity field $\mathbf{f}(\mathbf{x}, t)$ satisfies

$$\dot{\mathbf{x}} = \mathbf{f}(\mathbf{x}, t) \tag{21a}$$

$$\mathbf{x}(0) = \mathbf{x}_*, \tag{21b}$$

where the dot denotes differentiation with respect to time. When $\mathbf{f}$ is a function of $\mathbf{x}$, Eq. (21) is a nonlinear differential equation. Using polar coordinates $\mathbf{x} = (r, \vartheta)$, it follows that $\mathbf{f} = (u, v/r)$ and Eq. (21) becomes

$$\dot{r} = u \tag{22a}$$

$$\dot{\vartheta} = v/r \tag{22b}$$

$$[r(0), \vartheta(0)] = (r_*, \vartheta_*). \tag{22c}$$

Using the Eulerian velocity field (u, v) from Eq. (4), trajectories in Eq. (22) can be integrated numerically with an adaptive time step Runge–Kutta–Fehlberg algorithm (RKF45: see e.g., Maron and Lopez 1991), which satisfies a user-defined precision at each step. This is accomplished by adjusting the time step as a function of the difference between two Runge–Kutta schemes of order four and five, respectively, and allows the achievement of a prescribed precision on the integration of a trajectory over a given period while minimizing computational time.

Trajectories due to a Kelvin wave and a Poincaré wave are shown in Fig. 7 for the IBVP (or, equivalently, for the FP) and in Fig. 8 for the IP. According to their direction of propagation, the waves are seen to cause cyclonic (Kelvin wave) or anticyclonic loops (Poincaré wave) in the trajectories. While to first-order linear wave theory predicts zero mass transport, Longuet-Higgins (1969) showed that to second order the Lagrangian drift is given by the sum of the second-order Eulerian velocity and the Stokes drift. Wunsch (1973) showed, in particular for a Kelvin wave in a straight channel, that the second-order Eulerian velocity is in fact zero, leaving the Stokes drift as the sole contribution. The difference between a straight channel and a circular basin is due to Poincaré waves. While in a straight channel they are nearly standing and therefore produce no significant net drift (Wunsch 1973), in a circular basin they appear as progressive waves, whose Stokes drift can be important. This is particularly important when the duration of the wind is short compared to the dominant internal waves (Fig. 8), as in the IP case. Interestingly, due to the different radial structure of v of Kelvin and Poincaré waves (Fig. 1) and their opposite direction of propagation, the Stokes drift ends up being cyclonic for both waves.

If the geostrophic flow alone is considered, Eq. (21) becomes an autonomous nonlinear differential equation. Particles follow closed streamlines (Fig. 1) and no dispersion is possible. Dispersion can occur when unsteady perturbations are added. In this case the topology of the steady flow determines the spatial variability of dispersion (Binson 1997). For this reason it is of interest to study the structure of the geostrophic flow. Four fixed points can be found:

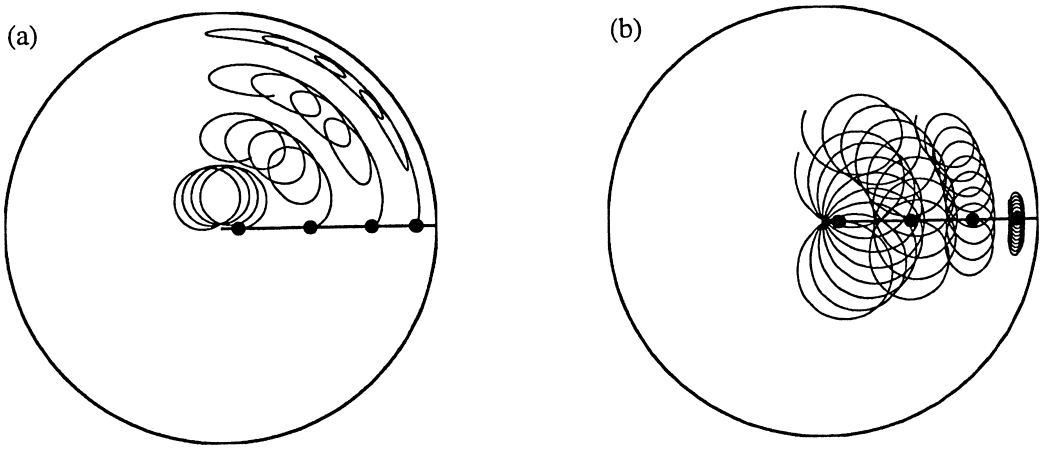

FIG. 8. Particle paths due to (a) the Kelvin wave and (b) the Poincaré wave generated from the IP for $S = 0.66$ and $W = 0.4$. Full circles indicate starting positions and trajectories are plotted for 4.4 inertial periods.

$$(r, \vartheta) = (S^{-1}, \pi/2), \quad (S^{-1}, 3\pi/2), \quad (r_c, 0), \quad (r_c, \pi), \tag{23}$$

where r_c satisfies $(\Delta_0 - rS)_{r=r_c} = 0$. Their stability is determined by the eigenvalues of the Jacobian matrix of the flow, which have been computed analytically making use of the frequency equation (A20). For $(r_c, 0)$ and (r_c, π) the eigenvalues are purely imaginary complex conjugate numbers, indicating these equilibrium points are stable: they are *elliptic points.* As will be seen by the study of Poincaré maps in section 5, elliptic points are surrounded by regions of regular motion even for very large forcing. The variation of r_c with the Burger number is given in Fig. 9. For $S \to 0$ the elliptic points are squeezed toward the shores, while for $S \to \infty$ a two-term Taylor expansion of the order zero and one modified Bessel functions for small arguments S^{-1} (Abramowitz and Stegun 1965) shows that $Sr_c \to 1/\sqrt{3}$. The fixed points at $(S^{-1}, \pi/2)$ and $(S^{-1}, 3\pi/2)$, on the other hand, have real distinct eigenvalues: they are unstable equilibria or *hyperbolic points.* Around them the effects of unsteady perturbations are felt first. It is interesting to note that the sediment redistribution patterns in Lake Kinneret show regions of sediment removal coinciding with the hyperbolic points of the geostrophic flow associated with the predominant westerly wind (Herman 1989). The streamlines connecting the hyperbolic points are called *separatrices*: for the circular basin they coincide with the north–south axis and the entire perimeter.

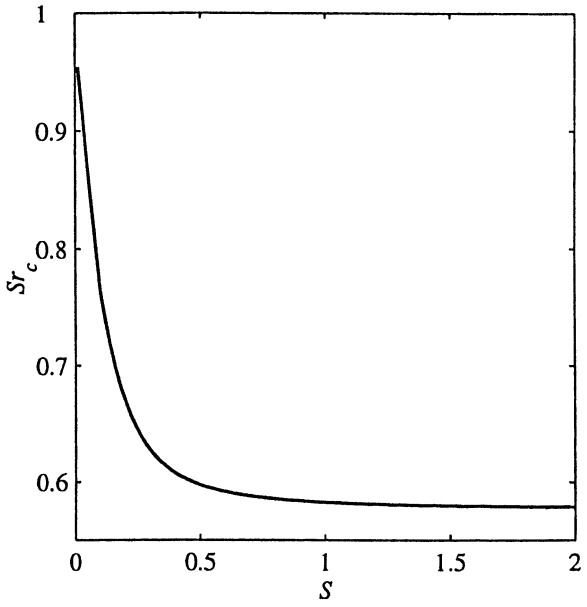

FIG. 9. Distance r_c of the elliptic points of the geostrophic flow from the center of the basin normalized by the size of the basin S^{-1}, as a function of the Burger number S. When $S \to \infty$, $Sr_c \to 1/\sqrt{3}$.

5. Dispersion properties of the mean flow

In this section the dispersion properties of the flow field Eq. (4) are investigated for the FP ($W_C \to \infty$, $W = W_F$) and the IBVP ($W_F \to \infty$, $W = W_C$). Since the linear velocity field is identical in the two cases provided W_F and W_C are equal and opposite (section 2), the transport properties will be the same. Here the problem will be approached from the point of view of *chaotic advection* (Aref 1984). The Poincaré-Bendixon theorem (Lichtenberg and Lieberman 1983) excludes the possibility of chaotic advection for two-dimensional differential systems that can be reduced to rest by a Galilean transformation, which is the case for the geostrophic flow or a single wave (Cox et al. 1990). However, the superposition of the geostrophic flow and a wave represents an unsteady two-dimensional flow, for which chaotic advection is in general possible (Binson 1996). Since this flow is periodic in time, Poincaré maps can be employed to study particle's orbits. For the present two-dimensional flow, where phase space and physical space coincide (Binson 1997), drawing Poincaré

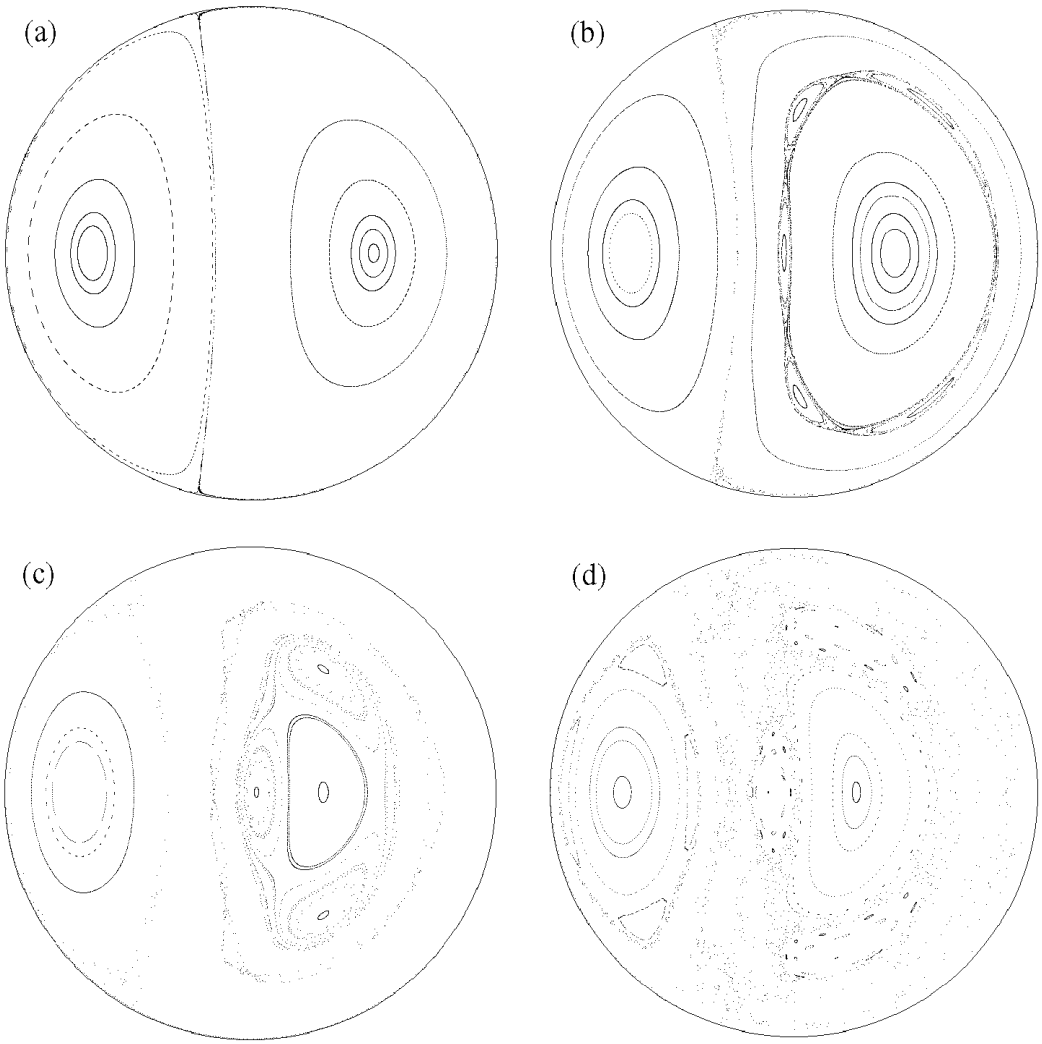

FIG. 10. Poincaré maps for the FP, for $S = 0.66$ and $W =$ (a) 0.16, (b) 0.10, (c) 0.07, and (d) 0.06. Only the geostrophic circulation and the Kelvin wave are considered. Eleven particles are released on the x axis and their position is drawn at time intervals equal to the Kelvin wave's period, for 800 periods.

maps involves releasing a number of particles and taking snapshots of their position at time intervals equal to the period of the wave, thus reducing the continuous flow to a discrete map. This has to be done for a large number of forcing periods (800 in our case) in order to detail the structure underlying the flow, but does not imply that the interpretation of this structure only applies to such large timescales.

Figure 10 shows Poincaré maps of the geostrophic flow perturbed by the Kelvin wave for several values of W. While W for these cases is so low as to invalidate the linearization in Eq. (1), these Poincaré maps are briefly discussed in order to understand the asymptotic effect of a perturbation on the geostrophic flow. At first, the Kelvin wave creates an asymmetry in the two gyres (Fig. 10a), reinforcing the cyclonic eastern gyre and squeezing the anticyclonic one toward the western shore. This causes a shift in the hyperbolic points, where chaotic advection first arises. The separatrices break up and trajectories tend to fill an area in the Poincaré map. This area grows as W decreases but does not affect the regions surrounding the elliptic points, which preserve their regularity. The structures that form between chaotic and regular regions are called KAM curves (Ottino 1989) and are first evident for $W = 0.10$ (Fig. 10b). Islands of regularity survive inside newly formed separatrices, which in turn break up as W decreases. KAM curves are typical of Hamiltonian systems, which preserve volume in phase space (Lichtenberg and Lieberman 1983). The present flow is Hamiltonian on average since the divergence of the velocity field in Eq. (4) vanishes only if averaged over the Kelvin wave's period.

At realistic values of W (≈ 1) the perturbation induced by the Kelvin wave appears too weak to cause any chaotic advection. However, dispersion can still be studied by computing the stretching of a small initial deviation

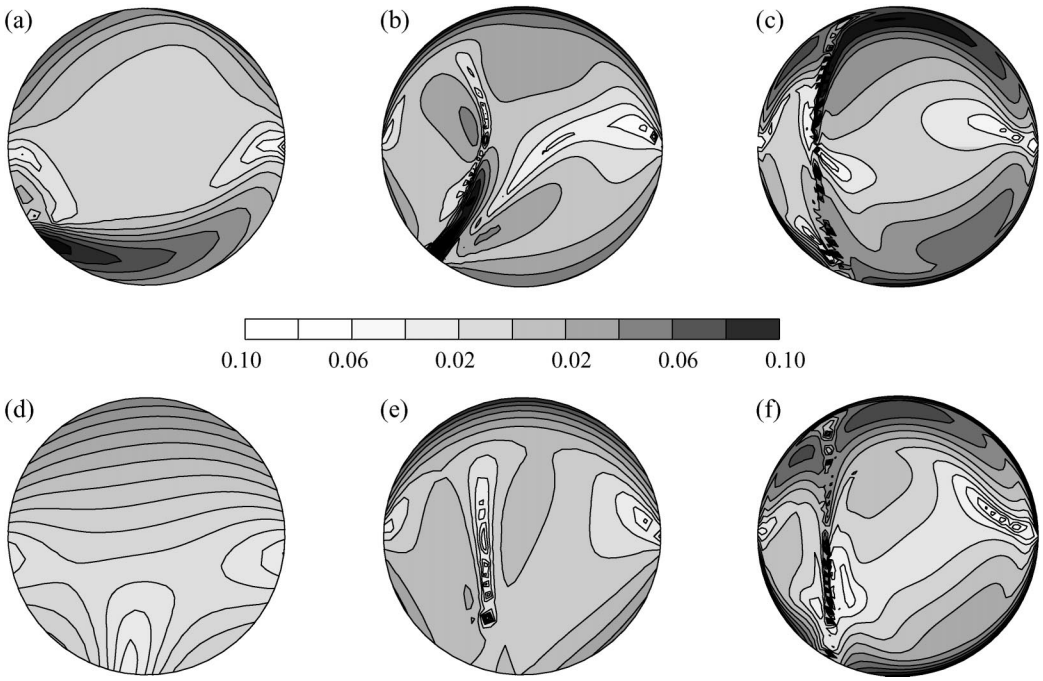

FIG. 11. The local Lyapunov exponent of surface layer trajectories due to the geostrophic circulation, the Kelvin wave, and the Poincaré wave computed for 4.8 inertial periods and normalized by the inertial frequency f. Only normal mode two is considered. In the upper row $W = 1$ and $S =$ (a) 0.1, (b) 0.3, and (c) 5. In the lower row $S = 0.66$ and $W =$ (d) 5, (e) 2, and (f) 1.

$\boldsymbol{\xi}(0)$ from a trajectory, which to first order is described by the *variational equation*

$$\dot{\boldsymbol{\xi}} = A(\mathbf{x}, t)\boldsymbol{\xi}, \tag{24}$$

where $A = \boldsymbol{\nabla}\mathbf{f}$ is the Jacobian matrix or rate of strain tensor of the flow from Eq. (21). The local Lyapunov exponent (Nese 1987; Eckhardt and Yao 1992),

$$\lambda_T = \frac{1}{T}\ln\frac{\|\boldsymbol{\xi}(T)\|}{\|\boldsymbol{\xi}(0)\|}, \tag{25}$$

describes the average rate of stretching experienced by $\boldsymbol{\xi}(t)$ over a time T. When $T \to \infty$, the standard Lyapunov exponent λ_∞ is recovered. A positive λ_∞ is a hallmark for chaotic advection (Binson 1997). For the chaotic trajectories of Fig. 10, λ_∞ is indeed positive, but it is zero everywhere in the basin for more realistic values of W; λ_T, on the other hand, retains the information of stretching rates over a finite time T, while also characterizing their spatial nonuniformity (Eckhardt and Yao 1992).

Local Lyapunov exponents have been computed for $T = 30$ ($\approx$five days at midlatitudes) for particles subject to geostrophic component, Kelvin wave, and Poincaré wave velocity fields contemporarily. A particle has been released for each cell of a grid laid over the basin, its trajectory computed for a time T, and the local Lyapunov exponent of that trajectory attributed to the initial cell. Then λ_T represents the average stretching rate encountered by the particle released in that cell. Eckhardt and Yao (1992) took a different approach, progressively assigning the local stretching rate to the cell traversed by the trajectory and thus characterizing stretching in a Eulerian sense. Here $\boldsymbol{\xi}(t)$ is computed by integrating Eq. (24) numerically along with the trajectory Eq. (22). The initial vector $\boldsymbol{\xi}(0)$ has length 1 and random orientation since any small displacement vector rotates into the direction of fastest growth (Eckhardt and Yao 1992; Dellago and Hoover 2000) within a relaxation time which has been verified to be small with respect to T. In order to avoid overflow, the length of $\boldsymbol{\xi}(t)$ is renormalized to 1 at regular time intervals, exploiting the linearity of Eq. (24). Here λ_T can be considered a consistent measure of spreading over timescales on the order of $T = 30$ since its spatial structure and magnitude attain a nearly constant value for times between 20 and 50.

A further qualitative description of dispersion is adopted by tracking each particle of an initially circular cloud. The main difference with respect to the computation of λ_T is due to the linearity implicit in Eq. (24), which limits λ_T to a measure of the stretching only for small initial deviations $\boldsymbol{\xi}(0)$. How much the behavior of a cloud changes when its size is finite depends on the spatial nonlinearity of the flow.

Figures 11a–c and 12 show the effect on λ_T of different values of S, while Figs. 11d–f and 13 represent the effect of W. A decrease in W or an increase in S both intensify the asymmetry in the two gyres in much the same way as shown by Poincaré maps (Fig. 10) and

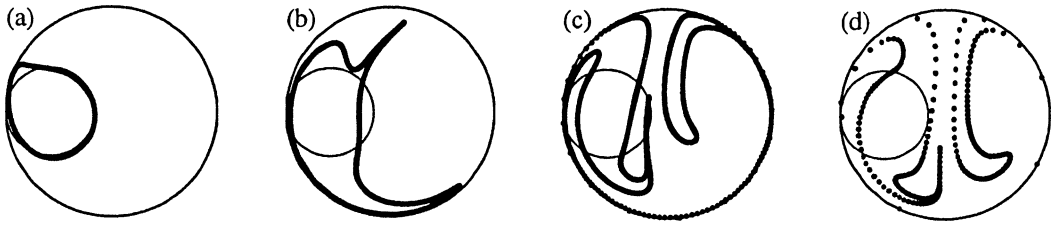

FIG. 12. The evolution of a cloud of particles in the surface layer (the thin circle to the left of the domain) for five inertial periods under the effect of the geostrophic flow, the Kelvin wave, and the Poincaré wave for $W = 1$ and $S = $ (a) 0.1, (b) 0.25, (c) 0.66, and (d) 2. Only normal mode two is considered.

increase the rate of stretching, mainly along the boundaries. This follows from the velocities in Eq. (4) being linearly proportional to SW^{-1}. In particular, the increase of dispersion rates with S is coherent with the increase of kinetic energy (Fig. 3). On the other hand, when the structure of the velocity field is examined independently of its amplitude, keeping SW^{-1} constant while changing S, it is seen from Fig. 14 that dispersion increases with rotation.

It is important to point out the effect of the waves in these considerations. Figure 15 shows λ_T for the geostrophic component alone. From comparison with Fig. 11c, it appears that the waves affect only marginally the magnitude of λ_T, implying that it is mainly the geostrophic component which is responsible for the stretching. However, the waves have two important effects. First, they trigger dispersion, since without waves, particles would follow closed streamlines and there would be no dispersion. Second, they modify the spatial distribution of λ_T, for example by inducing asymmetry in the two gyres. This is shown in Fig. 16: in a simple geostrophic flow, a cloud is not able to escape a gyre. Addition of the waves allows a portion of it to trespass the gyre's boundaries and to be further dispersed.

Since no diffusion is considered, the cloud's area remains constant on average, oscillating around its initial value due to the nonzero divergence of the waves. It is more interesting to track the evolution of the cloud's perimeter, which represents the exchange area with the surrounding fluid. The mechanism of stretching and folding observed in Figs. 12 and 13 is typical of chaotic advection, even though we have seen that for these values of W the perturbation induced by the waves is too small to actually cause chaotic advection. Nevertheless, the effect of this pseudochaotic advection is certainly a dramatic increase in exchange area, as shown in Fig. 17. Ignoring the oscillations induced by the waves, this growth is approximately linear.

6. Turbulent dispersion and advective spreading

It is of interest to compare pseudochaotic advection as presented in the previous sections to turbulent dispersion for the particular case of the surface layer of a stratified lake. Variables in this section will be dimensional except where specified otherwise. A simple way of comparing the two mechanisms, considered to act separately, is by determining the growth of the size $d(t)$ of a cloud. Extending the validity of the local Lyapunov exponents computed in section 5 to clouds of finite size as a first approximation, in a region characterized by a positive dimensionless λ_T a cloud of initial size d_0 grows like

$$d_{\text{adv}}(t) = d_0 e^{\lambda_T f t}. \tag{26}$$

A horizontal turbulent dispersion coefficient for a wind-driven surface layer can be estimated by taking the layer's depth h_1 as the characteristic length scale of turbulence (Csanady 1963) and the wind shear velocity u_* as the velocity scale (Monismith 1986, see appendix by J. Imberger and S. Monismith, 432–439):

$$K = Ch_1 u_*, \tag{27}$$

where C is a coefficient variable between 6 and 10, depending on the shape of the vertical velocity profile. The dispersion coefficient is independent of time and size of the patch since the cloud is considered to be larger than the largest scale of turbulent motion. Csan-

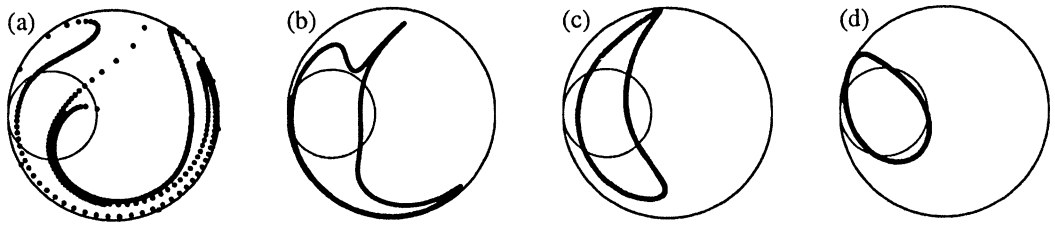

FIG. 13. The evolution of a cloud of particles in the surface layer (the thin circle to the left of the domain) for five inertial periods under the effect of the geostrophic flow, the Kelvin wave, and the Poincaré wave for $S = 0.25$ and $W = $ (a) 0.5, (b) 1, (c) 2, and (d) 10. Only normal mode two is considered.

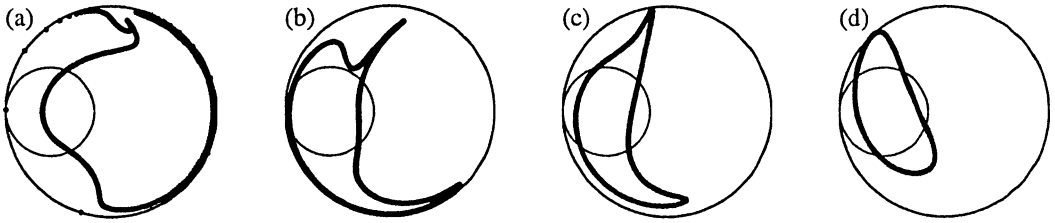

FIG. 14. The evolution of a cloud of particles in the surface layer (the thin circle to the left of the domain) for five inertial periods under the effect of the geostrophic flow, the Kelvin wave, and the Poincaré wave for S = (a) 0.1, (b) 0.25, (c) 0.66, and (d) 2 and W chosen such that $SW^{-1} = 0.25$ for each plot. Note that SW^{-1} is the amplitude of the velocity field. Only normal mode two is considered.

ady (1963), for example, observes the scale of turbulence in Lake Huron to be consistently of the order of 10 m, which is comparable to the surface layer depth. While for lakes with complex shorelines eddies of a range of scales can be generated (Ivey and Maxworthy 1992), for lakes with compact shapes Csanady's observation seems plausible since the surface layer depth is the only important length scale. The dispersion coefficient of a cloud whose standard deviation is σ is (Fischer et al. 1979)

$$K = \frac{1}{2}\frac{d\sigma^2}{dt}. \tag{28}$$

Equating the size of the cloud $d_{\text{turb}}(t)$ with σ, integrating Eq. (28), and substituting Eq. (27) for K yields

$$d_{\text{turb}}(t) = \sqrt{2Ch_1u_*(t + t_0)}, \tag{29}$$

where

$$t_0 = \frac{d_0^2}{2Ch_1u_*} \tag{30}$$

is a timescale related to the initial size of the cloud. Setting $d_{\text{turb}}(t_{\text{tr}}) = d_{\text{adv}}(t_{\text{tr}})$ from Eqs. (26) and (29) and solving for t_{tr} allows us to compute the transition time between small-scale turbulence dominated dispersion and pseudochaotic advection dominated dispersion. In terms of dimensionless time ($\tau_{\text{tr}} = t_{\text{tr}}f$ and $\tau_0 = t_0f$) this results in the implicit expression

$$\tau_{\text{tr}} = \tau_0(e^{2\lambda_T\tau_{\text{tr}}} - 1), \tag{31}$$

and is represented in Fig. 18 as a function of τ_0 and λ_T. Thus, for a cloud of a given initial size, λ_T maps the dispersion characteristics in the lake. Where its value is low, turbulent dispersion dominates for long times while, where it is high, the effect of large-scale motions is felt earlier. The latter dominates from $\tau = 0$ if the initial rate of growth in Eq. (26) is larger than that in Eq. (29), which translates into the condition $\lambda_T > \tau_0^{-1}/2$. On the other hand, turbulent dispersion dominates for $\tau \to \infty$ if the horizontal extent of the basin is smaller than $d_0e^{\lambda_T\tau_{\text{tr}}}$. As an example, a typical summer situation in Lake Kinneret sees a wind of 10 m s^{-1} blowing over a surface layer of 14-m thickness and $S \approx 2/3$. For clouds having an initial size of 100 and 200 m, $\tau_0 = 0.4$ and 11 inertial periods, respectively. From Fig. 11, there are large enough regions in the lake where $\lambda_T > 0.03$, yielding a transition time of $\tau_{\text{tr}} = 7.8$ and 2.1 inertial periods ($\approx$5.5 and 1.5 days at midlatitudes), respectively. The transition time is very sensitive to the initial size of the cloud, as expected from the exponential form of Eq. (26).

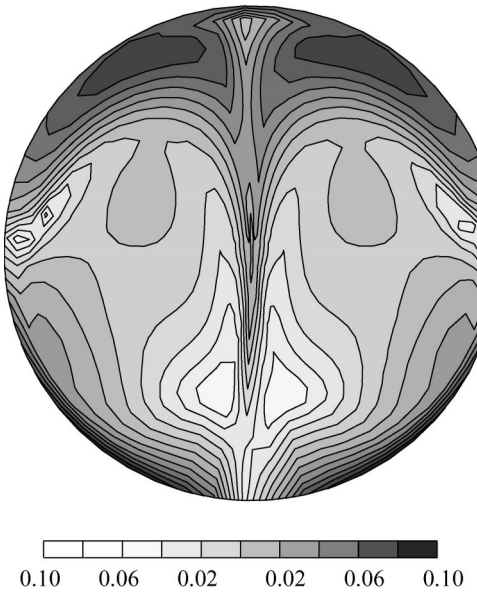

FIG. 15. The local Lyapunov exponent of surface layer trajectories due to the normal mode two geostrophic component computed for 4.8 inertial periods with $S = 0.66$ and $W = 1$. The Lyapunov exponent is normalized by the inertial frequency f.

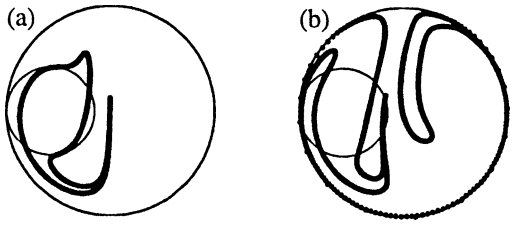

FIG. 16. The evolution of a cloud of particles in the surface layer (the thin circle to the left of the domain) for five inertial periods, with $S = 0.66$ and $W = 1$, under the effect of (a) the geostrophic flow alone and (b) with the Kelvin and Poincaré waves superimposed.

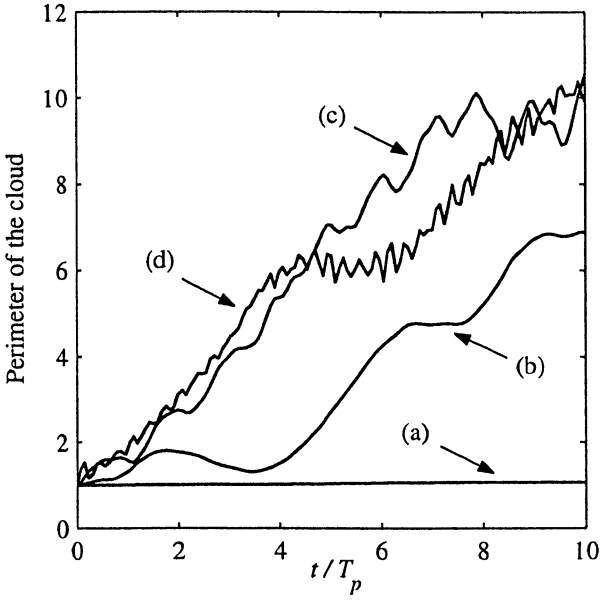

FIG. 17. Growth of the perimeter of the clouds of particles shown in Fig. 12. Time is normalized by the inertial period T_p and perimeters by their initial value.

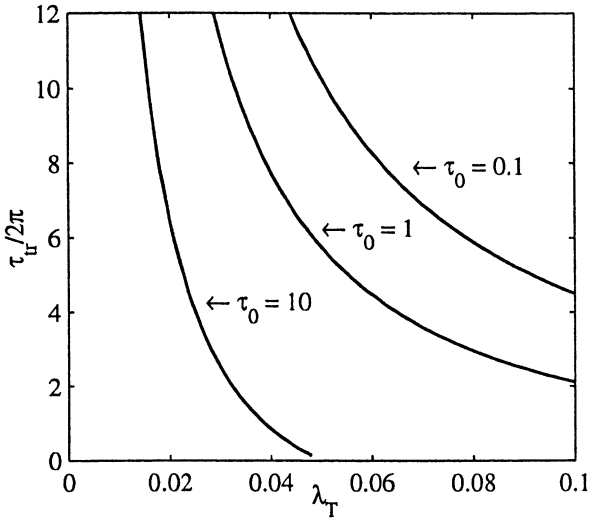

FIG. 18. Transition time τ_{tr} between turbulence dominated dispersion ($\tau < \tau_{tr}$) and mean advection dominated dispersion ($\tau > \tau_{tr}$), as a function of τ_0 and λ_T.

Small clouds are hardly affected by pseudochaotic advection but, if they are large enough, this mechanism can play a dominant role after a relatively small time.

7. Discussion

The structure of the motion which arises from an initial tilt in a rotating basin is very different from the simple seiche that develops in the nonrotational case ($S \rightarrow \infty$). The rotation of the earth splits the initial setup into a geostrophic component and a set of cyclonic and anticyclonic waves. For each of the waves, the potential to kinetic energy ratio given by Antenucci and Imberger (2001) applies. However, the total energy in the basin is not equal to the sum of the energy of the waves since there is also a geostrophic component as part of the solution, both for the IBVP and the FP. For low Burger numbers the geostrophic component dominates, storing most of its energy in potential form. This is ultimately due to the difficulty in converting potential to kinetic energy in rotating flows (Gill 1982) and causes the potential to kinetic energy ratio for the basin as a whole to increase with decreasing Burger number. The fact that no initial potential energy is available in the FP is responsible for the difference in the geostrophic displacements with respect to the IBVP.

The interpretation in terms of potential vorticity developed in section 3d sheds light on the differences in the higher order transport properties of the two cases. In particular, the imposition of an initial tilt in the IBVP introduces a potential vorticity gradient. Due to conservation of potential vorticity, the motion of fluid columns results in the generation of relative vorticity and ultimately eddies. These eddies transport mass very effectively, leading to strong horizontal mixing. This implies that for the IBVP trajectories computed in section 5 are accurate for times smaller than the time of formation of the eddies. In other words, the relative vorticity produced due to conservation of potential vorticity generates velocities that can be of the same order as the Stokes drift. For a general IBVP, there is no potential vorticity gradient *only* if the initial condition is a superposition of natural wavelike modes since each of them has a zero potential vorticity gradient.

On the other hand, it is likely that the forced problems more accurately describe the behavior of real basins. In this case, no initial potential vorticity gradient is supplied and none is introduced by the uniform forcing. Thus, the linear velocity field exactly satisfies the nonlinear evolution equation of potential vorticity (section 3d) and therefore no eddies form as fluid columns move. We therefore expect the dispersion properties derived through linear theory to hold for longer times in the forced problems than in the IBVP. In general, however, the potential vorticity of a flow can be modified also due to a curl in the wind forcing, whose importance for the circulation in a closed basin was pointed out in a numerical study of Lake Tahoe by Strub and Powell (1986), or due to generation at the boundaries. The latter, in particular, was observed by Ivey and Maxworthy (1992) in their experiments on Kelvin waves dissipation. In the absence of any background potential vorticity gradient, they introduced relative vorticity by letting Kelvin waves interact with a sharp edge in the shoreline topography. The flow separating from the edge generated large scale two dimensional eddies, again responsible for enhanced horizontal mixing.

The Stokes drift of all waves is cyclonic, independent of their direction of propagation and can be of significant

magnitude. However, advection is due predominantly to the geostrophic component, which can exhibit chaotic advection when perturbed by the Kelvin wave for small Wedderburn numbers. For realistic values of W, Poincaré maps do not reveal any chaotic advection due to the weakness of the perturbation induced by the Kelvin wave. However, in a real basin other perturbation factors (e.g., shoreline topography, secondary circulations) may act on the geostrophic flow to generate chaotic advection.

For realistic values of W, local Lyapunov exponents (Fig. 11) allow us to get an estimate of the dispersion rates once the Wedderburn number and the Burger number of a basin are known. Figures 11a–c show, for instance, that for lakes having the same stratification, forcing, and latitude, but different horizontal dimension, the smaller lake exhibits stronger dispersion. When the role of stratification is studied, results have to be interpreted with care since both W and S are dependent on stratification. As an example, the seasonal evolution of a stratified lake can be crudely simplified by assuming a two-layer stratification with uniform constant densities and the same forcing throughout the year. In spring the surface layer deepens, causing both S and W to increase. Given the proportionality of the surface layer velocities to SW^{-1}, this causes two counteracting effects on dispersion, suggesting that spring dispersion rates are very sensitive to small changes in the stratification or forcing. In fall, the surface layer usually continues to deepen, yielding a similar picture of dispersion, unless the surface layer itself is already thicker than the lower layer. In this case, W would keep increasing but S would decrease, causing dispersion rates to fade quickly.

When the waves are added to the geostrophic flow, the boundaries of the gyres act no longer as an impermeable barrier to transport. This has the important effect of stretching and folding the cloud, thereby dramatically increasing the exchange area with the surrounding fluid. This increase is approximately linear. It is interesting to note that for the growth of dye filaments in a field of homogeneous turbulence Batchelor (1952) also predicted a linear increase in time. This points to an important difference between the two mechanisms. While turbulent dispersion increases the area of the cloud and has an actual mixing effect, pseudochaotic advection only increases the exchange area, thereby not directly mixing the cloud but only enhancing the effect of smaller-scale mixing mechanisms, such as molecular or turbulent dispersion.

When the variable bathymetry of a real lake is taken into account, its response includes an additional set of topographic waves (e.g., Birchfield and Hickie 1977; Huang and Saylor 1982), found by Huang and Saylor (1982) to be significant mainly near resonance conditions. Besides, both the geostrophic component and the Kelvin and Poincaré waves are modified by the variable depth, precluding a straightforward extension of the energetics presented above. Furthermore, the full solution of the problem in this case is complicated by the difficulty of applying normal mode decomposition to a stratified basin with nonuniform depth. On the other hand, it is worth noting that our fundamental conclusions on horizontal transport hold unchanged in this case. Indeed, we showed that enhanced transport due to chaotic advection is exhibited already by a single wave perturbing the geostrophic motion. Addition of further modes, be it Poincaré waves or topographic waves, will only strengthen this dispersion mechanism.

8. Conclusions

The solution to the IBVP of a rotating, stratified basin subject to a linear initial tilt of an interface has been derived and compared to forced cases. The limit for impulsive forcing has also been obtained, revealing that shorter forcing events do not set up any geostrophic motion and favor Poincaré waves over Kelvin waves.

The initial setup in the IBVP involves the existence of a potential vorticity gradient that ultimately leads to the generation of eddies. We expect the timescale for the generation of these eddies to be of several days. This mechanism is absent in the forced problems since there is no initial setup and the forcing is uniform. The difference between the two forced cases consists in the geostrophic circulation, which is present in the FP to balance the stress acting on the surface but is absent in the IP. In particular, in the FP the geostrophic component accounts for half the total energy in the response for all Burger numbers. The difference between the geostrophic circulation in the FP and in the IBVP is due to conservation of potential vorticity.

When the Burger number is small, Poincaré waves are negligible in the energy balance. The geostrophic component is dominant in the IBVP, while the response is pushed to the boundaries in the FP. When the Burger number is large, the geostrophic component vanishes in the IBVP, while it reduces to a setup with no associated circulation in the FP.

The geostrophic flow is responsible for advection in the basin. For $W > 1$, the local Lyapunov exponent is an indicator of the importance of pseudochaotic advection over turbulent dispersion in different regions of the basin. Turbulent dispersion is dominant for short timescales and small clouds, while pseudochaotic advection sets in after longer times or for larger clouds, provided the cloud is in a region characterized by large stretching rates. In a lake, the transition time between the two mechanisms can be as low as one day. The important conclusion is that in field experiments the dispersion of a cloud is linked not only to the strength of the turbulent eddy field, but can partly be explained in an entirely deterministic manner by considering the topology of the large-scale flow field.

Acknowledgments. We thank Jason Antenucci for interesting discussions on internal wave generation; Gian-

carlo Benettin, Francesco Fassó, and Gary Froyland for valuable explanations about the world of dynamical systems; Robb McDonald for comments on potential vorticity; and Chris Dallimore, Geoff Wake, and two anonymous reviewers for constructive comments on the manuscript. Author R.S. gratefully acknowledges an Ing. Guglielmo Marin scholarship and an Ing. Aldo Gini scholarship. This paper forms Centre for Water Research reference ED 1625-RS.

APPENDIX

Solution of the Fundamental Problem

In order to decouple the solution procedure in space and time, the Laplace transform of Eq. (1) is taken. Transformed displacements are defined as

$$\Pi = L(\eta) = \int_0^\infty \eta(\tau)e^{-s\tau}\, d\tau, \tag{A1}$$

where s is the parameter of the transformation. Similarly, U and V are the Laplace transforms of u and v, respectively. When time derivatives are transformed, the initial conditions come into play:

$$\begin{aligned} L\left(\frac{\partial \eta}{\partial \tau}\right) &= \int_0^\infty \frac{\partial \eta}{\partial \tau} e^{-s\tau}\, d\tau \\ &= \eta(\tau)e^{-s\tau}|_0^\infty + s\int_0^\infty \eta(\tau)e^{-s\tau}\, d\tau \\ &= -\eta(\tau = 0) + s\Pi. \end{aligned} \tag{A2}$$

In transforming the forcing term, the Laplace transform s^{-1} of the Heaviside function $H(\tau)$ is used. The equations of motion and conservation of mass Eq. (1) are transformed as

$$sU - V = -\frac{\partial \Pi}{\partial r} + \frac{1}{s}SW_F^{-1}\cos\vartheta \tag{A3a}$$

$$sV + U = -\frac{\partial \Pi}{r\partial \vartheta} - \frac{1}{s}SW_F^{-1}\sin\vartheta \tag{A3b}$$

$$\frac{U}{r} + \frac{\partial U}{\partial r} + \frac{\partial V}{r\partial \vartheta} = -s\Pi + \eta_0. \tag{A3c}$$

These can be combined to derive a wave equation in terms of transformed displacements only. Multiplying the divergence of Eqs. (A3a) and (A3b) by s, adding the curl of the same two equations, and making use of Eq. (A3c) yields

$$\nabla^2\Pi = (1 + s^2)\left(\Pi - \frac{\eta_0}{s}\right), \tag{A4}$$

where the Laplacian in polar coordinates is

$$\nabla^2 \equiv \frac{\partial^2}{\partial r^2} + \frac{\partial}{r\partial r} + \frac{\partial^2}{r^2\partial \vartheta^2}. \tag{A5}$$

The next task is to express the boundary condition of zero radial velocity at $r = S^{-1}$ in terms of the displacement. Multiplying Eq. (A3a) by s, adding Eq. (A3b), and setting $U = 0$ at $r = S^{-1}$ yields

$$\begin{aligned} s\frac{\partial \Pi}{\partial r} + \frac{\partial \Pi}{r\partial \vartheta} \\ = SW_F^{-1}\left(\cos\vartheta - \frac{\sin\vartheta}{s}\right)0 : r = S^{-1}. \end{aligned} \tag{A6}$$

Note how the initial condition enters the wave equation (A4), while the forcing enters the boundary condition (A6). A solution to Eq. (A4) is now sought in the form of the sum of all azimuthal modes, each one having its own radial structure:

$$\Pi = \sum_{n=0}^{\infty} G_n^c(r)\cos n\vartheta + \sum_{n=1}^{\infty} G_n^s(r)\sin n\vartheta. \tag{A7}$$

Substituting this expression into the transformed wave equation (A4), one finds that the radial structure of each azimuthal mode must obey a Bessel equation:

$$\frac{\partial^2 G}{\partial r^2} + \frac{\partial G}{r\partial r} - \left(z^2 + \frac{n^2}{r^2}\right)G = 0, \tag{A8}$$

which has the solution (Abramowitz and Stegun 1965)

$$G(r) = KI_n(zr), \tag{A9}$$

where K is a constant, $z = (1 + s^2)^{1/2}$, and I_n represents the modified Bessel function of order n; G represents all G_n^c and G_n^s, except G_1^c, which instead, due to the initial condition Eq. (3), satisfies the nonhomogeneous Bessel equation

$$\begin{aligned} \frac{\partial^2 G_1^c}{\partial r^2} + \frac{\partial G_1^c}{r\partial r} - \left(1 + s^2 + \frac{1}{r^2}\right)G_1^c \\ = -\frac{1 + s^2}{s}SW_C^{-1}r. \end{aligned} \tag{A10}$$

The particular solution to Eq. (A10) is readily found, and the general solution for G_1^c is therefore

$$G_1^c(r) = K_1^c I_1(zr) + \frac{SW_C^{-1}r}{s}. \tag{A11}$$

In general, Eq. (A7) is substituted into the boundary condition Eq. (A6) and one equation for each harmonic in ϑ is found, allowing the coefficients in Eq. (A7) to be determined. However, due to the azimuthal mode one initial condition, Eq. (A7) will contain only terms in $\cos\vartheta$ and $\sin\vartheta$. Substituting this reduced expression for Eq. (A7) into Eq. (A6) and solving separately for the coefficients of $\cos\vartheta$ and $\sin\vartheta$ yields two equations for the coefficients K_1^c and K_1^s. These are then substituted back into Eq. (A7) to yield

$$\Pi = \frac{\Phi(s)}{\Psi(s)}, \tag{A12}$$

where

$$\Phi(s) = SW_c^{-1}r(1 + M^2s^2)\cos\vartheta - (W_C^{-1} - W_F^{-1})\frac{I_1(zr)}{I_1(z)} \times [(1 + Ms^2)\cos\vartheta + s(1 - M)\sin\vartheta] \quad \text{(A13)}$$

$$\Psi(s) = s(1 + M^2s^2) \quad \text{(A14)}$$

$$M = \frac{zI_0(z)}{I_1(z)} - 1, \quad \text{(A15)}$$

and $z(s)$ is complex in general so as to avoid the use of both Bessel and modified Bessel functions. The inverse Laplace transform, defined as

$$\eta(\tau) = L^{-1}(\Pi) = \frac{1}{2\pi i}\int_{-i\infty}^{+i\infty}\Pi(s)e^{s\tau}\,ds, \quad \text{(A16)}$$

is then applied to Eq. (A12) to find the solution in terms of the actual displacements. Using Heaviside's formula (Csanady 1968), which applies to functions that can be written as a quotient of two polynomials, the inverse Laplace transform can be computed as

$$\eta(\tau) = \sum_i \frac{\Phi(s_i)}{\Psi'(s_i)}e^{s_i\tau}, \quad \text{(A17)}$$

where the prime denotes differentiation with respect to s and the poles s_i are the zeros of Ψ in Eq. (A14). The poles are of two kinds:

$$s = 0 \quad \text{(A18)}$$

$$s = \pm i\sigma_k, \quad \text{(A19)}$$

where the indices have been dropped. The first pole generates a steady geostrophic component, while the poles associated with the natural frequencies of the basin σ_k give rise to progressive waves. The frequencies σ_k satisfy the dispersion relationship (Csanady 1967)

$$1 - \sigma_k^2M^2 = 0, \quad \text{(A20)}$$

where

$$M = \frac{z_kI_0(z_k)}{I_1(z_k)} - 1 \quad \text{(A21)}$$

$$z_k = S^{-1}\sqrt{1 - \sigma_k^2}. \quad \text{(A22)}$$

The solution for displacements follows after some algebra and is given in Eq. (4a), where

$$a_k = \frac{\sigma_k - 1}{1 + \sigma_k - S^{-2}\sigma_k^3} \quad \text{(A23)}$$

$$A_k = \frac{I_1(rz_kS)}{I_1(z_k)} \quad \text{(A24)}$$

$$\Delta_k = r\frac{dA_k}{dr} = \frac{rz_kSI_0(rz_kS)}{I_1(z_k)} - A_k \quad \text{(A25)}$$

$$\sigma_0 = 0. \quad \text{(A26)}$$

Velocities [Eqs. (4b,c)] can then be found by deriving an expression for transformed velocities from Eq. (A3a,b) in terms of transformed displacements and by inverting them again through Heaviside's formula Eq. (A17).

REFERENCES

Abramowitz, M., and I. A. Stegun, 1965: *Handbook of Mathematical Functions: With Formulas, Graphs, and Mathematical Tables.* Dover, 1046 pp.

Antenucci, J. P., and J. Imberger, 2001: Energetics of long internal gravity waves in large lakes. *Limnol. Oceanogr.*, **46,** 1760–1773.

Aref, H., 1984: Stirring by chaotic advection. *J. Fluid Mech.*, **143,** 1–22.

Batchelor, G. K., 1952: The effect of turbulence on material lines and surfaces. *Proc. Roy. Soc. London*, **A213,** 349–366.

Binson, J., 1996: Chaotic advection by Rossby–Haurwitz waves. *Fluid Dyn. Res.*, **18,** 1–16.

——, 1997: Chaotic mixing by internal inertia–gravity waves. *Phys. Fluids*, **9,** 945–962.

Birchfield, G. E., 1969: Response of a circular model Great Lake to a suddenly imposed wind stress. *J. Geophys. Res.*, **74,** 5547–5554.

——, and B. P. Hickie, 1977: The time-dependent response of a circular basin of variable depth to a wind stress. *J. Phys. Oceanogr.*, **7,** 691–701.

Cox, S. M., P. G. Drazin, S. C. Ryrie, and K. Slater, 1990: Chaotic advection of irrotational flows and of waves in fluids. *J. Fluid Mech.*, **214,** 517–534.

Csanady, G. T., 1963: Turbulent diffusion in Lake Huron. *J. Fluid Mech.*, **17,** 360–384.

——, 1966: Accelerated diffusion in the skewed shear flow of lake currents. *J. Geophys. Res.*, **71,** 411–420.

——, 1967: Large-scale motion in the Great Lakes. *J. Geophys. Res.*, **72,** 4151–4162.

——, 1968: Motions in a model Great Lake due to a suddenly imposed wind. *J. Geophys. Res.*, **73,** 6435–6447.

——, 1982: On the structure of transient upwelling events. *J. Phys. Oceanogr.*, **12,** 84–96.

Dellago, C., and W. G. Hoover, 2000: Are local Lyapunov exponents continuous in phase space? *Phys. Lett. A*, **268,** 330–334.

Eckhardt, B., and D. Yao, 1992: Local Lyapunov exponents in chaotic systems. *Physica D*, **65,** 100–108.

Fischer, H. B., E. J. List, R. C. Y. Koh, J. Imberger, and N. H. Brooks, 1979: *Mixing in Inland and Coastal Waters.* Academic Press, 483 pp.

Gill, A. E., 1982: *Atmosphere–Ocean Dynamics.* Academic Press, 662 PP.

Herman, G., 1989: The time dependent response of Lake Kinneret to an applied wind stress and hydraulic flow: Advection of suspended matter. *Arch. Hydrobiol.*, **115,** 41–57.

Huang, J. C. K., and J. H. Saylor, 1982: Vorticity waves in a shallow basin. *Dyn. Atmos. Oceans*, **6,** 177–196.

Imberger, J., 1998: Flux paths in a stratified lake: A review. *Physical Processes in Lakes and Oceans*, J. Imberger, Ed., Coastal and Estuarine Studies, Vol. 54, Amer. Geophys. Union, 1–17.

Ivey, G. N., and T. Maxworthy, 1992: Mixing driven by internal Kelvin waves in large lakes and the coastal oceans. *Proc. 11th Australasian Fluid Mechanics Conf.*, Hobart, Australia, University of Tasmania, 303–306.

Lamb, H., 1932: *Hydrodynamics*, 6th ed. Dover, 738 pp.

Lawrence, G. A., K. I. Ashley, N. Yonemitsu, and J. R. Ellis, 1995: Natural dispersion in a small lake. *Limnol. Oceanogr.*, **40,** 1519–1526.

Lichtenberg, A. J., and M. A. Lieberman, 1983: *Regular and Stochastic Motion.* Springer-Verlag, 499 pp.

List, E. J., G. Gartrell, and C. D. Winant, 1990: Diffusion and dispersion in coastal waters. *J. Hydraul. Eng.*, **11,** 1158–1179.

Longuet-Higgins, M. S., 1969: On the transport of mass by time varying ocean currents. *Deep-Sea Res.*, **16,** 431–448.

Maron, M. J., and R. J. Lopez, 1991: *Numerical Analysis: A Practical Approach.* 3d ed. Wadsworth, 743 pp.

Monismith, S. G., 1985: Wind-forced motions in stratified lakes and their effect on mixed layer shear. *Limnol. Oceanogr.,* **30,** 771–783.

——, 1986: An experimental study of the upwelling response of stratified reservoirs to surface shear stress. *J. Fluid Mech.,* **171,** 407–439.

Mortimer, C. H., 1952: Water movements in lakes during summer stratification: Evidence from the distribution of temperature in Windermere. *Philos. Trans. Roy. Soc. London,* **A236,** 355–404.

Murthy, C. R., 1975: Dispersion of floatables in lake currents. *J. Phys. Oceanogr.,* **5,** 193–195.

Nese, J. M., 1987: Quantifying local predictability in phase space. *Physica D,* **35,** 237–250.

Okubo, A., 1971: Oceanic diffusion diagrams. *Deep-Sea Res.,* **18,** 789–802.

Ostrovsky, I., Y. Z. Yacobi, P. Walline, and I. Kalikhman, 1996: Seiche induced mixing: Its impact on lake productivity. *Deep-Sea Res.,* **41,** 323–332.

Ottino, J. M., 1989: *The Kinematics of Mixing: Stretching, Chaos and Transport.* Cambridge University Press, 364 pp.

Pedlosky, J., 1979: *Geophysical Fluid Dynamics.* Springer-Verlag, 624 pp.

Ridderinkhof, H., and J. T. F. Zimmerman, 1992: Chaotic stirring in a tidal system. *Science,* **258,** 1107–1111.

Serruya, S., E. Hollan, and B. Bitsch, 1984: Steady winter circulations in Lake Constance and Kinneret driven by wind and main tributaries. *Arch. Hydrobiol.,* **1,** 33–110.

Spigel, R. H., and J. Imberger, 1980: The classification of mixed-layer dynamics in lakes of small to medium size. *J. Phys. Oceanogr.,* **10,** 1104–1121.

Strub, P. T., and T. M. Powell, 1986: Wind-driven surface transport in stratified closed basins: Direct versus residual circulations. *J. Geophys. Res.,* **91,** 8497–8508.

Veronis, G., 1956: Partition of energy between geostrophic and non-geostrophic oceanic motions. *Deep-Sea Res.,* **3,** 157–177.

Wunsch, C., 1973: On the mean drift in large lakes. *Limnol. Oceanogr.,* **18,** 793–795.

Zimmerman, J. T. F., 1986: The tidal whirlpool: A review of horizontal dispersion by tidal and residual currents. *Neth. J. Sea Res.,* **20,** 133–154.